Bioprinted mesenchymal stem cell microfiber-derived extracellular vesicles alleviate unilateral renal ischemia-reperfusion injury and fibrosis by inhibiting tubular epithelial cells ferroptosis

Qiang Guo [a,b,1], Jianwei Chen [c,1], Jianjian Wu [a,b], Zijun Mo [a,b,1], Lei Ye [a,b], Wenwen Zhong [a,b], Yi Zhang [d], Huajian Lai [a,b], Yifei Zhang [a,b], Jianguang Qiu [a,b,*], Tao Xu [c,e,**], Dejuan Wang [a,b,***]

[a] Department of Urology, The Sixth Affiliated Hospital, Sun Yat-sen University, No 26 Yuancun Erheng Road, Guangzhou, 510655, China
[b] Biomedical Innovation Center, The Sixth Affiliated Hospital, Sun Yat-sen University, Guangzhou, 510655, China
[c] Bio-intelligent Manufacturing and Living Matter Bioprinting Center, Research Institute of Tsinghua University in Shenzhen, Tsinghua University, Shenzhen, 518057, China
[d] Department of Research and Development, Huaqing Zhimei (Shenzhen) Biotechnology Co., Ltd., Shenzhen, Guangdong Province, 518107, China
[e] Tsinghua Shenzhen International Graduate School, Tsinghua University, Shenzhen 518055, China

ARTICLE INFO

ABSTRACT

Renal unilateral ischemia-reperfusion injury (UIRI) constitutes a significant global health challenge, with poor recovery leading to chronic kidney disease and subsequent renal fibrosis. Extracellular vesicles (EVs) present substantial potential benefits for renal diseases. However, the limited yield and efficacy of EVs produced through traditional methodologies (2D-EVs) severely restrict their widespread application. Moreover, the efficient and effective strategies for using EVs in UIRI treatment and their mechanisms remain largely unexplored. In this study, we propose an innovative approach by integrating bioprinted mesenchymal stem cell microfiber extracellular vesicles production technology (3D-EVs) with a tail vein injection method, introducing a novel treatment strategy for UIRI. Our comparison of the biological functions of 2D-EVs and 3D-EVs, both in vitro and in vivo, reveals that 3D-EVs significantly outperform 2D-EVs. Specifically, in vitro, 3D-EVs demonstrate a superior capacity to enhance the proliferation and migration of NRK-52E cells and mitigate hypoxia/reoxygenation (H/R)-induced injuries by reducing epithelial-mesenchymal transformation, extracellular matrix deposition, and ferroptosis. In vivo, 3D-EVs exhibit enhanced therapeutic effects, as evidenced by improved renal function and decreased collagen deposition in UIRI mouse kidneys. We further elucidate the mechanism by which 3D-EVs derived from KLF15 ameliorate UIRI-induced tubular epithelial cells (TECs) ferroptosis through the modulation of SLC7A11 and GPX4 expression. Our findings suggest that bioprinted mesenchymal stem cells microfiber-derived EVs significantly ameliorate renal UIRI, opening new avenues for effective and efficient EV-based therapies in UIRI treatment.

1. Introduction

Mesenchymal stem cell-derived extracellular vesicles (MSC-EVs) exhibit anti-inflammatory, antioxidative, anti-apoptotic properties, and promote cell proliferation, migration, and neovascularization. These vesicles, which encapsulate MSC-originated RNA, proteins, and lipids, show promise in mitigating various renal diseases [1,2]. For instance, extracellular vesicles from human bone marrow MSCs (BM-MSCs) can halt the progression of acute kidney injury (AKI) by facilitating the transition of macrophages from the M1 to the M2 phenotype [3]. Similarly, EVs from umbilical cord MSCs (UC-MSCs) reduce inflammation and renal oxidative stress by modulating the p38/MAPK pathway [4]. Additionally, adipose-derived MSCs (AD-MSCs) produce extracellular vesicles that carry miR-342–5p, which inhibits TLR9 activation and supports renal regeneration [5]. These results underscore the potential of MSC-EVs in the effective management of renal injuries. Nevertheless, the current limitations in EVs yield, production efficiency, therapeutic potency, and delivery strategy considerably hinder their broader adoption [6,7]. Furthermore, the efficacy of advanced MSC-EVs production techniques in treating unilateral renal ischemia-reperfusion injury (UIRI) remains to be fully explored.

Previous studies have identified two innovative approaches for enhancing extracellular vesicles production efficiency: hollow fiber technology and microcarrier combined with tangential flow filtration. Hollow fiber technology facilitates the cultivation of cells in large quantities, up to an order of 10^9, and boosts extracellular vesicle production by 20-fold, compared to traditional 2D culture methods [8]. The microcarrier approach attaches cells to plastic microsphere surfaces within a stirring system, increasing the cell load per volume and, through tangential flow filtration, augments EV yield by 141-fold [9]. These advancements underscore the significant impact of the culture environment on cell properties and the molecular composition of EVs, thereby influencing their functional and therapeutic potential [10]. This study introduces a novel, high-efficiency EV production technology that merges coaxial bioprinted microfiber cultivation of mesenchymal stem cells with a tail vein injection technique for treating (UIRI). The microfiber exhibits a unique core-shell microstructure and we termed the produced extracellular vesicles as 3D-EVs. This arrangement not only facilitates a "tissue-like" assembly of cells but also yields EVs with distinct protein content and superior cargo quality compared to traditional methods (2D-EVs). Specifically, this method has been shown to increase the production of EV particles by approximately 1000 times per defined medium volume, enhancing both the quantity and quality of EVs [11]. Nevertheless, the application of these advanced EV production methods in disease treatment, particularly UIRI, remains limited, and the influence of cultivation environment changes on EV cargo content and its role in UIRI repair warrants further investigation.

A substantial body of evidence indicates that inhibiting ferroptosis can ameliorate ischemic organ damage and fibrosis, thereby proposing a novel therapeutic strategy for preventing ischemic injury [12,13]. Furthermore, numerous studies have underscored the critical role of ferroptosis in UIRI-induced AKI, particularly noting that renal tubular epithelial cells (TECs) are the most adversely affected by ferroptosis [14]. Therefore, modulating the ferroptosis pathway in TECs through the application of MSC-EVs emerges as a vital approach for potentially improving the long-term renal outcomes following UIRI. Nonetheless, the specific functions and mechanisms through which bioprinted MSC microfiber-derived 3D-EVs regulate UIRI remain to be elucidated.

In this study, we introduce a novel approach by integrating coaxial bioprinted mesenchymal stem cell microfiber-derived extracellular vesicles production technology with the tail vein injection method to treat UIRI. Expanding upon our innovative strategy, we would like to explore whether 3D-EVs have a better therapeutic effect than 2D-EVs in the treatment of UIRI (Fig. 1). Our observations reveal that 3D-EVs offer superior therapeutic benefits compared to 2D-EVs, irrespective of the in vitro or in vivo setting. Further examination into the therapeutic mechanisms of 3D-EVs in UIRI indicates that 3D-EVs have an enhanced effect, potentially by delivering Krüppel-like factor 15 (KLF15) to mitigate ferroptosis in TECs, thereby presenting a new avenue in the development of treatments for UIRI.

2. Materials and methods

2.1. Cell culture

The human adipose-derived MSCs were purchased from the Chinese Academy of Science and cultured in MSCM (Mesenchymal stem cell culture medium) with 10 % FBS (fetal bovine serum) and 1 % penicillin/streptomycin at 37 °C with 5 % CO2. Rat renal tubular epithelium cells (NRK-52E) were purchased from the Chinese Academy of Science and cultured in DMEM (Dulbecco's Modified Eagle Medium) containing 1 g/L glucose with 10 % FBS at 37 °C with 5 % CO2. To induce hypoxia, we placed cells in a hypoxic chamber with 5 % CO2, 94 % N2, and 1 % O2 at 37 °C for 2 h, followed by reoxygenation for 24 h. The dosage of extracellular vesicles used in the cell experiments was 5×10^8 particles/ml unless otherwise specified [15]. All the cell lines were authenticated by STR profiling and tested clean for mycoplasma contamination.

2.2. Isolation and characterization of 2D-EVs and 3D-EVs

2D MSCs culture and 2D-EVs extraction as described previously [11]. We used the coaxial bioprinting technology for the cultivation of AD-MSCs and the production of 3D-EVs (Fig. 1), as we previously reported [11]. Briefly, the alginate material and MSCs are extruded by a double-layer coaxial needle to form a cell-encapsulating microfiber. After the microfiber was fabricated, the media of MSCs was changed to an FBS-free medium for 24 h or 48 h and collected. Regardless of 2D, or microfiber cell culture, we expanded the primary ADMSC to the 5th generation, at which time the number of cells was about 1*10^9, and collected cell culture-conditioned medium continuously for 5 days. All conditioned mediums were stored at −80 °C and exosomes were
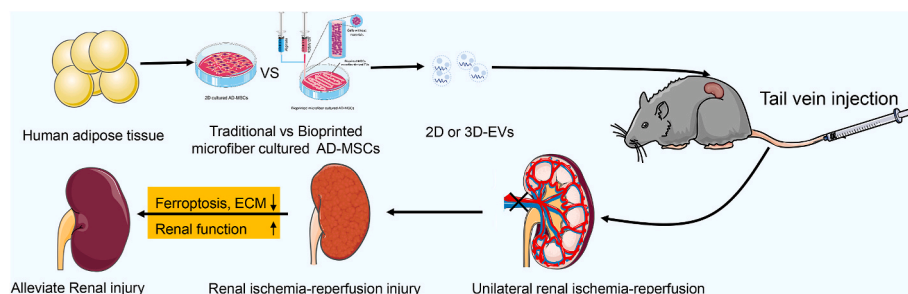

Fig. 1. Schematic diagram of combining bioprinted mesenchymal stem cell microfiber-derived extracellular vesicles production technology (3D-EVs) and tail vein injection to treat UIRI induced renal injury.

extracted as soon as the supernatant was collected. 2D- and 3D-EVs were purified and collected by differentiation ultracentrifugation as described previously. Briefly, we first at $300 \times g$ for 10 min, and $2000 \times g$ for 30 min to eliminate fragments and dead cells, then 10, $000 \times g$ for 30 min to remove impurities such as microvesicles. The supernatant was filtered through a 0.22 μm filter (SLGV033RS, Millipore, USA) to remove vesicles or protein aggregates. Then the supernatant was spun at 100, $000 \times g$ for 70 min. The resulting pellet was washed with PBS and spun at 100, $000 \times g$ for 70 min. After that, the pellet was resuspended by PBS for further identification. Protein concentration of extracellular vesicles ($2*10^{10}$ particles, 50ul) was examined by BCA assay (CWBIO, Beijing, China) and subjected to western blot analysis for CD81 (ABclonal, A5270), CD63 (Abcam, ab68418), Calnexin (ABclonal, A15631), TSG101 (Abcam, ab125011), and Goat anti-Rabbit IgG Peroxidase Conjugated (Abcam). We observed the size and structure of extracellular vesicles with a transmission electron microscope (TEM) (Hitachi, 120kv, Japan), and nanoparticle tracking analysis (NTA; Particle Metrix, Germany).

2.3. Fluorescence labeling of extracellular vesicles

PKH26-labeled extracellular vesicles were incubated with NRK-52E for 24 h, washed three times with PBS, and fixation with 4 % paraformaldehyde, the cells were stained with DAPI and then photographed under a confocal microscope.

2.4. Cell viability assay

For NRK-52E cell viability assay, NRK-52E cells were seeded into 96-well plates at $2.5*10^3$ cells/well. Before the cell viability assay, we placed cells in a hypoxic chamber for 2 h or not, followed by reoxygenation for 24 h to induce H/R treatment. After that, the cells were divided into Ctrl, H/R, H/R+2D-EVs, and H/R+3D-EVs groups. 6 wells were set up for each group. Cell counting kit-8 (CCK-8) reagent of 10 μl was added into 96-well plates at 24 h, 48 h, and 72h. After incubating in a 37 °C incubator away from light for 2 h, the absorbance at 450 nm was measured by a microplate reader to compare cell proliferation in each group. For MSCs viability assay, MSCs viability in the microfiber was assessed using a fluorescent live/dead assay kit (KeyGEN BioTECH, Nanjing, China) following the manufacturer's protocol. Briefly, the medium was removed and washed three times with PBS. Cell fibers were then immersed in PBS mixed with 8 μM propidium iodide and 2 μM calcein-AM. Cell fibers were incubated at 37 °C in the dark for 15 min and washed three times with PBS. Images were obtained using a fluorescence microscope (Eclipse Ti2-U, Nikon, Japan) with green (live) and red (dead).

2.5. Wound healing assay

NRK-52E cells were plated in six-well plates at $5*10^5$ cells/well. When cell confluence reached 80 %, the medium was removed and washed three times with PBS and starved with FBS-free medium. Then a sterile 200 μl pipette tip was used to scratch the confluent cell monolayer and divide it into Ctrl, H/R, H/R+2D-EVs, and H/R+3D-EVs groups. Images were taken at 0 h, 24 h after the monolayer was scratched. The migrated area was quantified using ImageJ software: Migration area (%) = (A0 - An)/A0 × 100 %, where A0 is the initial wound area (t = 0 h) and An is the remaining wound area at the time of measurement (t = n h).

2.6. Transwell assay

A density of $1*10^4$ NRK-52E cells was seeded into the upper chamber of a Transwell insert (Corning, 3422), while 600 μl of either fresh medium or extracellular vesicles-enriched culture supernatant containing 10 % FBS was added to the lower chamber. Cells were treated with PBS, H/R, H/R+2D-EVs, and H/R+3D-EVs and incubated for an additional 24 hours. Subsequently, the migrating cells that had traversed the basolateral membrane were fixed with 4 % paraformaldehyde and stained with 0.1 % crystal violet. Cellular invasion was visualized and documented using an optical microscope (Nikon, Japan).

2.7. Enzyme-linked immunosorbent assay (ELISA)

Protein expression levels for KLF15 in MSCs and 3D-EVs were using the Human KLF15 (Kruppel Like Factor 15) ELISA Kit (ELK, ELK4227) following the manufacturer's instructions.

2.8. Western blot

Protein was extracted from NRK-52E, or tissues utilizing RIPA lysis buffer (Solarbio, Beijing, China) in the presence of protease inhibitors. The concentrations of protein samples were determined by BCA assay (CWBIO). Proteins were separated by 10 % SDS-PAGE gel electrophoresis and transferred to polyvinylidene difluoride membranes (PVDF, Millipore). Next, the membrane was blocked with 5 % milk at room temperature. The membrane with blotted protein was incubated with primary antibodies against GAPDH (Servicebio, GB12002), SLC7A11 (ABclonal, ab37185), FTH-1 (Affinity, DF6278, USA), GPX4 (ABclonal, ab125066), Fibronectin (ABclonal, A12932), Collagen I (ABclonal, a16891), E-cadherin (CST, 24E10, USA), Vimentin (CST, D21H3), α-SMA (ABclonal, A1011), KLF15 (ABclonal, A13420) diluted with primary antibody diluent was added and incubated at 4 °C overnight. The diluted HRP-conjugated secondary antibodies (Abcam) were added and incubated at room temperature for 1 h. Finally, the protein bands were visualized utilizing enhanced chemiluminescence reagents (GBCBIO, China) and quantified by Image J software.

2.9. qRT-PCR

RNA from NRK-52E or kidney tissues was collected utilizing a total RNA kit (Omega) following the manufacturer's instructions. cDNA was synthesized from the RNA using Evo M-MLV RT Kit with gDNA Clean for qPCR (Accurate Biology, China). Then qRT-PCR assays were performed using SYBR green (Accurate Biology). Relative gene expression normalized to GAPDH was calculated using the $2{-}\Delta\Delta Ct$ method. All primers were synthesized by Tsingke (Beijing Tsingke Biotech Co., Ltd.) and listed in Supplementary Table 1. There were three replicates per group.

2.10. Immunocytochemistry

NRK-52E was planted on a confocal dish and added different treatments. After treatment, NRK-52E was fixed in 4 % paraformaldehyde for 10 min, then blocked with 5 % BSA at room temperature for 1 h. After that, NRK-52E was hybridized with primary antibodies at 4 °C overnight and visualized with fluorescence-labeled secondary antibodies (Beyotime, China) for 1h at 37 °C. DAPI was used to stain nuclei at room temperature. Images were captured using a confocal microscope (Nikon, Tokyo).

2.11. Animal model

The male C57BL/6J mice were purchased from the Experimental Animal Center of Sun-Yat sen University and were randomly allocated into the sham group, UIRI model group, UIRI + Fer-1 group, UIRI + 2D-EVs group, and UIRI + 3D-EVs group (n = 5 per group) using the random number table method. A UIRI model was established according to a previous study. Specifically, the mice model of renal UIRI was established by clamping the pedicles for 30 minutes followed by reperfusion without contralateral nephrectomy. 2D- and 3D-EVs were applied three times through tail vein injection, each time with 3×10^9 particles on days 1, 4, and 7 [16,17]. The kidneys of mice were removed at 14 days

after UIRI and kidney tissues were collected for various analyses. All experiments involving animals were conducted according to the ethical policies and procedures approved by the ethics committee of the sixth affiliated hospital of Sun-Yat Sen University (Approval no. IACUC-2021092902).

2.12. Blood urea nitrogen and serum creatinine assay

Creatinine and urea nitrogen concentrations in serum were measured using the Creatinine (Cr) Assay kit and blood urea nitrogen Assay (BUN) kit following the manufacturer's instructions. These two kits were purchased from Nanjing Jiancheng Bioengineering Institute.

2.13. Histology evaluation, immunohistochemical and immunofluorescence staining

Mouse kidneys were fixed in 4 % paraformaldehyde and embedded in paraffin. Paraffin was cut into sections and mounted on glass slides, deparaffinized with xylene, dehydrated through a graded series of ethanol, and stained with hematoxylin-eosin. The tubules were evaluated according to the following scoring system: 0 = no tubular injury; 1 = 10 % or fewer tubules injured; 2 = 11–25 % tubules injured; 3 = 26–50 % tubules injured; 4 = 51–74 % tubules injured; and 5 = 75 % or more tubules injured. To evaluate collagen deposition, sections were stained with Masson's Trichrome. For immunohistochemical staining, the sections were incubated with primary antibodies overnight at 4 °C. The sections were then washed and incubated at room temperature with a horseradish peroxidase (HRP) conjugated secondary antibody. For immunofluorescence staining, slide-mounted tissues were blocked with 5 % BSA for 1h and then incubated overnight at 4 °C with primary antibodies, followed by staining with corresponding secondary antibodies at room temperature. Cell nuclei were stained with DAPI. Images were captured using a confocal microscope (Nikon, Tokyo). The acquired mages were quantified by Image J software.

2.14. Perls' staining

The kidney sections or NRK-52E were fixed in 4 % paraformaldehyde and washed three times, then incubated in freshly prepared Perls' solution (1:1, 5 % potassium ferrocyanide and 5 % HCl) for 1 h, followed by washing with phosphate-buffered saline (PBS). A second incubation was then performed in 0.5 % diamine benzidine tetrahydrochloride. After rinsing, the sections were observed under a light microscope.

2.15. Determination of reactive oxygen species generation

The DCFH-DA probe (Sigma-Aldrich, MO, USA) was used to determine the generation of intracellular ROS. Briefly, the cells were treated with PBS, H/R, H/R + 2D-EVs, and H/R + 3D-EVs for 4 h before incubation with DCFH-DA (5 μM) at 37 °C for 30 min. Finally, the stained cells were analyzed with a confocal microscope.

2.16. Iron concentration and MDA assay

A total of 10 mg renal tissues for each group were cut and washed with cold PBS and then homogenized by vibrating homogenizer immediately. For NRK-52E cells, the collected cells were homogenized by the ultrasonic cell disrupter. The relative iron and MDA concentrations in renal tissues and NRK-52E cell lysates were assessed using an iron assay kit (Jiancheng Bioengineering Institute, Nanjing, China) and Micro Malondialdehyde Assay Kit (Solarbio, Beijing, China) according to the manufacturer's instructions.

2.17. Determination of renal GSSG/GSH ratio

The ratio of oxidized glutathione (GSSG) to total glutathione (GSH, reduced GSH + GSSG) was determined by GSH and GSSG Assay Kit (Beyotime, China) according to the manufacturer's instructions. The absorbance at 412 nm was measured by a microplate reader.

2.18. Plasmid and siRNA transfection

KLF15 cDNA overexpression plasmid and small interfering RNA (siKLF15) were purchased from Tsingke (Beijing Tsingke Biotech Co., Ltd.), and siRNA sequences were provided in Supplementary Table 2. NRK-52E was seeded to 80 % confluence in 6-well plates in triplicate. Lipofectamine 3000 (Life Technologies) reagent was used to transfect KLF15 plasmid or siKLF15 oligos into NRK-52E. Cell protein or RNA samples were harvested at 48 h after transfection and processed for western blot or qRT-PCR analysis.

2.19. Statistical analysis

Data are presented as means ± SD (standard deviation). The student's t-test used GraphPad Prism version 9.0 software to analyze the statistical significance between the two groups. One-way analysis of variance (ANOVA) followed by Dunnett was used for studies involving more than two groups. A two-sided P < 0.05 was considered statistically significant.

3. Results

3.1. Culture of AD-MSCs and the characterization of 2D-EVs and 3D-EVs

The schematic representation of MSCs cultured in a traditional 2D environment compared to those bioprinted in 3D is illustrated in Fig. 2A. Following the extrusion of MSC microfibers, we employed both standard and confocal microscopy for characterization, revealing that AD-MSCs encapsulated within the fiber cores adopted a round morphology, with some forming spheroids, as depicted in Fig. 2Bi. Notably, live/dead staining indicated a high survival rate, approximately 90.3 %, highlighting the 3D environment's effectiveness in facilitating dense cell survival and enhancing interactions among adjacent cells (Fig. 2Bii). In the process of characterizing extracellular vesicles (EVs), we extracted, purified, and analyzed EVs from the MSC medium, confirming the presence of a characteristic dish-shaped, double-layer membrane structure in both 2D-EVs and 3D-EVs, ranging in diameter from 30 to 150 nm (Fig. 2C and D). Furthermore, the expression of CD81, CD63, and TSG101, recognized markers of EVs, was prominently observed, confirming the successful purification of these vesicles (Fig. 2E). Subsequently, the 2D- and 3D-EVs were labeled with PKH-26, a lipophilic fluorescent dye, and incubated with NRK-52E cells, resulting in the uptake of labeled EVs by tubular cells, as shown in Fig. 2F.

3.2. 3D-EVs exhibited enhanced abilities to promote the proliferation and migration of NR-52E cells in vitro

To investigate the impact of 2D-EVs and 3D-EVs on H/R-induced injuries in NRK-52E cells, we performed a series of experiments, including cell counting kit-8 (CCK-8), wound healing, transwell migration, and western blot assays for validation. Results, depicted in Fig. 3A and B, demonstrated that H/R significantly reduced the viability and proliferating cell nuclear antigen (PCNA) expression in NRK-52E cells. Conversely, treatments with 2D-EVs and 3D-EVs significantly restored cell viability and PCNA expression, with 3D-EVs exhibiting superior therapeutic effects over 2D-EVs. Notably, 3D-EVs demonstrated enhanced efficacy in facilitating migration recovery compared to 2D-EVs. The results of the wound healing assay are shown in Fig. 3C, the percentage of wound closure area was significantly increased from 63.02 ± 1.4 to 71.76 ± 1.43 and 79.4 ± 1.61 after 2D- and 3D-EVs treatment, respectively; at the same time, the H/R+3D-EVs group had less residual area than the H/R+2D-EVs group and had a significant
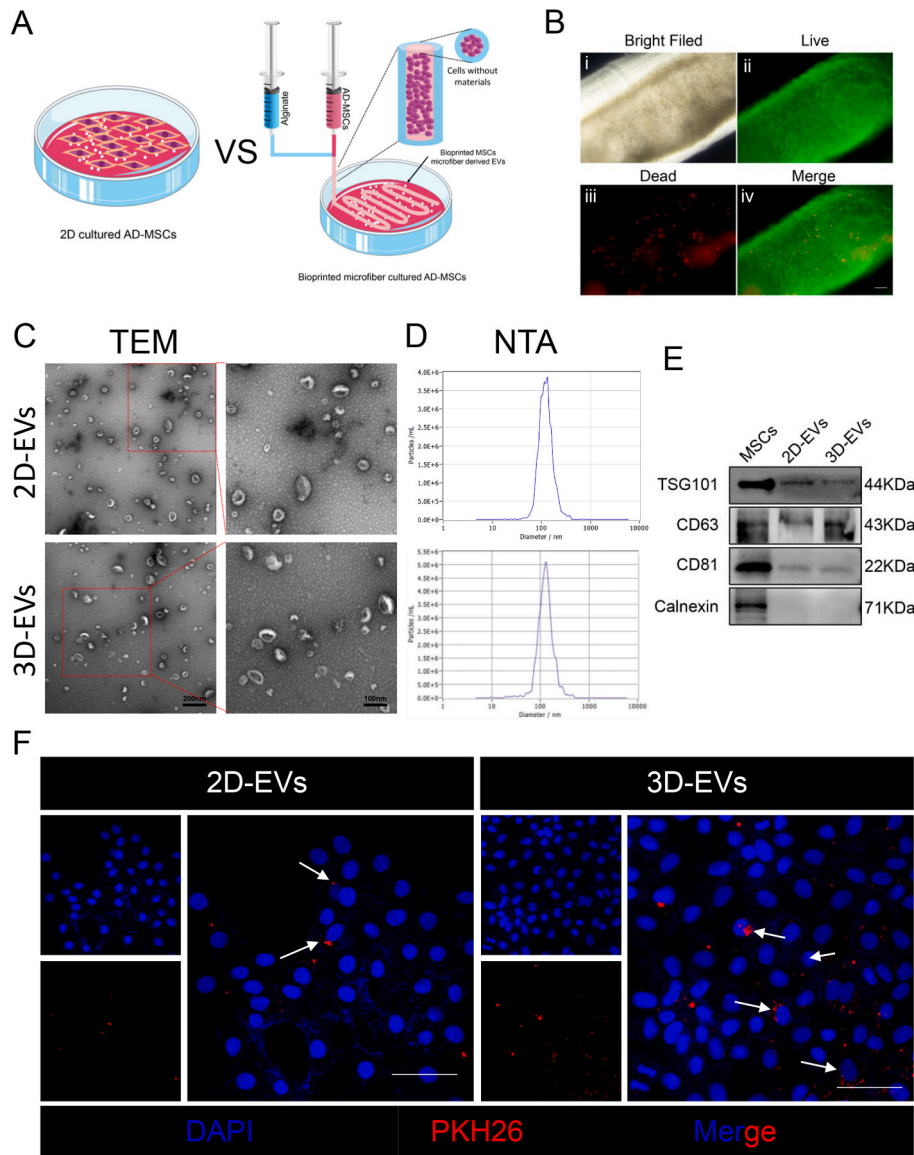
Fig. 2. Culture of AD-MSCs and the Characterization of 2D-EVs and 3D-EVs. A. Schematic diagram of traditional 2D-EVs and bioprinted MSC microfiber-derived extracellular vesicles. **B.** The Bright filed and live/dead staining of AD-MSCs in 3D microfibers. **C.** TEM of 2D-EVs and 3D-EVs. **D.** Representative graph of EVs size distribution by Nanoparticle tracking system. **E.** Western blot analysis showing the presence of EVs markers (CD81, CD63, TSG101, and Calnexin) in purified MSCs supernatants. **F.** Fluorescent staining confirms the intracellular transfer of 2D- and 3D-EVs in NRK-52E cells. EVs were labeled with PKH-26 (red) and incubated with NRK-52E cells for 24 h, followed by immunofluorescence staining for DAPI (blue). Arrows indicate EVs. Scale bar = 50 μm.

difference (p < 0.01) (Fig. 3D), revealed that H/R markedly impaired cell migration, and 3D-EVs has a better ability to facilitate migration than 2D-EVs. Then transwell results showed that 2D- and 3D-EVs significantly mitigated the H/R-induced inhibition of cell migration (cell number = 80.67 ± 10.4) (Fig. 3E), the H/R+3D-EVs group (n = 173.33 ± 19.35) had more number of migrated cells than the H/R+2D-EVs group (n = 229 ± 8.72) and had a significant difference (p < 0.01) (Fig. 3F), further indicated that 3D-EVs has a better ability to facilitate migration. Moreover, upon inducing NRK-52E cells with H/R and treating them with either type of extracellular vesicles, we observed that both could ameliorate H/R-induced epithelial-mesenchymal transformation (EMT), with 3D-EVs providing more pronounced amelioration than 2D-EVs (Fig. 3G). These findings underscore the superior therapeutic potential of 3D-EVs over 2D-EVs in alleviating H/R-induced injuries in NRK-52E cells in vitro.

3.3. 3D-EVs exert better therapeutic effects on renal injury than 2D-EVs in vivo

To explore the therapeutic potential of 2D-EVs and 3D-EVs in treating unilateral renal ischemia-reperfusion injury (UIRI), a UIRI mouse model was established, and animals were subsequently treated with these extracellular vesicles (Fig. 4A). Fourteen days post-surgery, mice were euthanized to collect samples. As depicted in Fig. 4B–D, UIRI resulted in significant renal atrophy and injury, evidenced by marked elevations in creatinine and blood urea nitrogen levels. Conversely, administering 2D-EVs and 3D-EVs ameliorated UIRI-induced renal atrophy and impaired renal function, with 3D-EVs demonstrating enhanced therapeutic efficacy. More specifically, 2D- and 3D-EVs decreased UIRI-induced serum creatinine (2.48 ± 0.44 mg/dl) to 1.25 ± 0.06 mg/dl and 0.78 ± 0.12 mg/dl, respectively, whereas blood urea nitrogen decreased from 154.30 ± 6.68 mg/dl to 113 ± 8.26 mg/dl and 98.33 ± 7.99 mg/dl. Additionally, WB and qPCR analyses indicated that UIRI notably promoted EMT and extracellular matrix
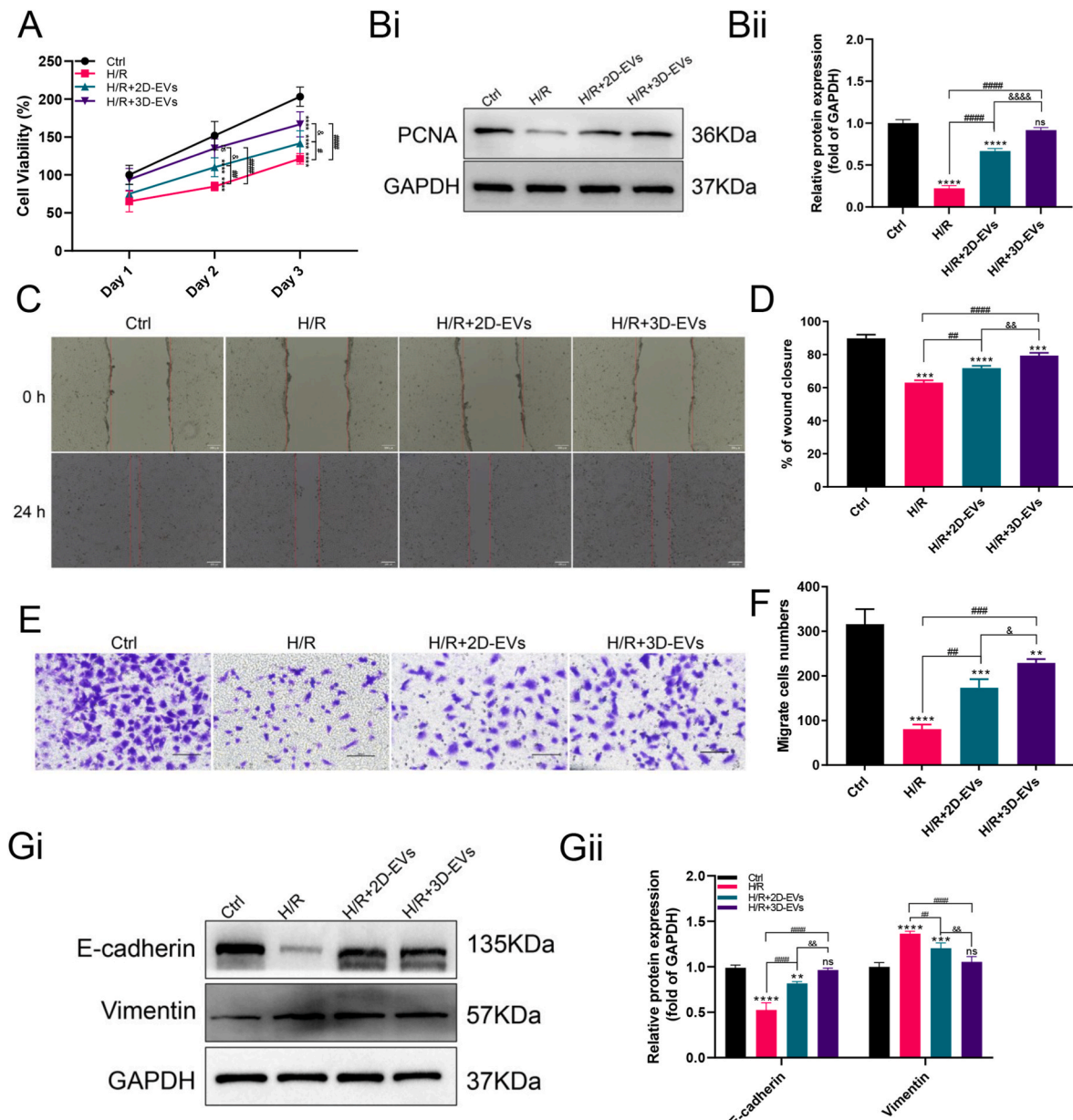
Fig. 3. 3D-EVs exhibited enhanced abilities to promote the proliferation and migration of NR-52E cells in vitro. A. The NRK-52E cell viability after different treatments. **B.** Representative Western blotting (Bi) and quantitative data (Bii) show the protein expression of PCNA in H/R induced NRK-52E after 2D-EVs and 3D-EVs treated. Relative expressions were expressed as fold induction over controls after normalization with GAPDH. ns and ****P < 0.0001 vs ctrl; ####P < 0.0001 vs H/R group; &&&&P < 0.0001 vs H/R+3D-Exos group; ns, not significant (n = 3). **C, D.** Representative wound healing images (C) and quantitative data (D) show the migration ability of NRK-52E after different treatments. Relative expressions were expressed as fold induction over controls. ***P < 0.001 and ****P < 0.0001 vs ctrl; ##P < 0.001, ####P < 0.0001 vs H/R group; &&P < 0.01 vs H/R+3D-EVs group; (Scale bar = 200um, n = 3). **E, F.** Representative cell migration images (E) and quantitative data (F) show the migration ability of NRK-52E after different treatments. Relative expressions were expressed as fold induction over controls. **P < 0.05, ***P < 0.001 and ****P < 0.0001 vs ctrl; ##P < 0.001, ###P < 0.001 vs H/R group; &P < 0.05 vs H/R+3D-EVs group; (Scale bar = 100um, n = 3). **G.** Representative Western blotting (Gi) and quantitative data (Gii) show the protein expression of E-cadherin and Vimentin in H/R induced NRK-52E after 2D-EVs and 3D-EVs treated. Relative expressions were expressed as fold induction over controls after normalization with GAPDH. **P < 0.01, ***P < 0.001 and ****P < 0.0001 vs ctrl; ##P < 0.001, ####P < 0.0001 vs H/R group; &&P < 0.01 vs H/R+3D-EVs group; ns, not significant (n = 3).

deposition, effects that were effectively reduced by treatments with 2D-EVs and 3D-EVs, particularly by 3D-EVs (Fig. 4E and F). Histological examinations further verified that UIRI-related tubular injuries (tubular dilatation marked by "*", glomerular atrophy marked by "#"), extracellular matrix buildup, and EMT were significantly mitigated by both vesicle types, with 3D-EVs showing superior therapeutic outcomes (Fig. 4G). Specifically, the application of 2D- and 3D-EVs resulted in a decrease in the UIRI-induced tubular injury score from 2.67 ± 0.5 to 1.78 ± 0.44 and 1 ± 0.7; while the percentage of collagen deposition

was reduced from 57.84 ± 4.4 to 32.15 ± 3.87 and 12.26 ± 0.98, respectively. The quantitative profiles of E-cadherin and Vimentin also illustrate that 3D-EVs have better remission of UIRI-induced EMT than 2D-EVs. These findings show the superior efficacy of 3D-EVs over 2D-EVs in vivo.

3.4. UIRI induces ferroptosis in renal tubular epithelial cells

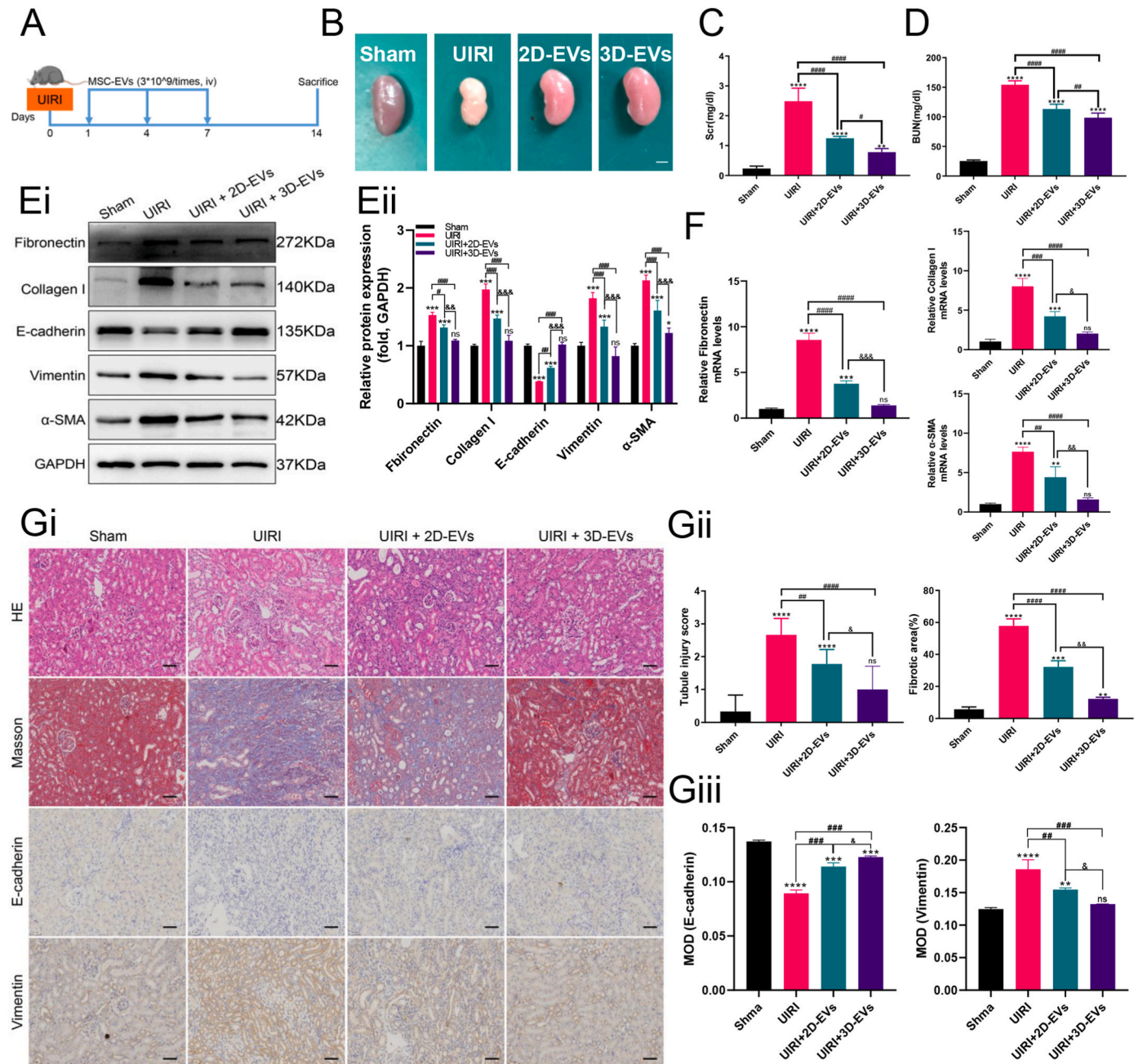Ferroptosis plays a critical role in the pathogenesis of renal ischemia-

Fig. 4. 3D-EVs exert better therapeutic effects on renal injury than 2D-EVs in vivo. A. Diagram shows the animal experimental design. Blue arrows indicate the time points when 2D-EVs or 3D-EVs (3*10^9 particles/times) were injected intravenously. **B.** The gross appearance of kidneys (Scale bar = 2 mm). **C, D.** Serum creatinine (C) and blood urea nitrogen (D) levels in different groups as indicated (n = 3). **E.** Representative Western blotting (Ei) and quantitative data (Eii) show the protein expression of Fibronectin, Collagen I, α-SMA, E-cadherin, and Vimentin after 2D-EVs and 3D-EVs treated UIRI kidney. Relative expressions were expressed as fold induction over sham controls after normalization with GAPDH. *P < 0.05, **P < 0.01, ***P < 0.001 and ****P < 0.0001 vs sham; #P < 0.05, ##P < 0.001, ####P < 0.0001 vs UIRI group; &P < 0.05 and &&&&P < 0.0001 vs UIRI+3D-EVs group; ns, not significant (n = 3). **F.** mRNA expression of Fibronectin, Collagen I, and α-SMA in UIRI, 2D-EVs, and 3D-EVs treated mice kidneys were measured by qRT-PCR (n = 3). **G.** Representative images (Gi) and quantitative data of HE (tubular dilatation marked by "*", glomerular atrophy marked by "#"), Masson staining (Gii), and immunohistochemical staining for E-cadherin and Vimentin (Giii) in UIRI, 2D-EVs, and 3D-EVs treated mice kidneys. Scale bar = 50um.

reperfusion injury, renal fibrosis, and renal cancer [14]. To investigate the link between renal ischemia-reperfusion injury and ferroptosis, we administered Fer-1 [18], a specific inhibitor of ferroptosis by eliminating lipid hydroperoxides, in a UIRI mouse model (Fig. 5A). Observations revealed that 30 minutes of renal ischemia followed by reperfusion impaired renal function, as indicated by elevated serum creatinine and plasma urea nitrogen levels (Fig. 5B and C), and HE displayed tubular injury with dilation (Fig. 5D). However, these adverse

effects were mitigated following Fer-1 administration. Furthermore, the rate of cell apoptosis, significantly elevated in the UIRI group, was reduced after Fer-1 treatment, as determined by TUNEL staining (Fig. S1). Central regulators of ferroptosis, SLC7A11, and GPX4, typically serve as markers for this process [19]. Generally, ferroptosis leads to decreased expression of SLC7A11 and GPX4, both of decreased will lead to more severe kidney injury and fibrosis. Immunohistochemical analyses demonstrated a significant reduction in SLC7A11 and GPX4
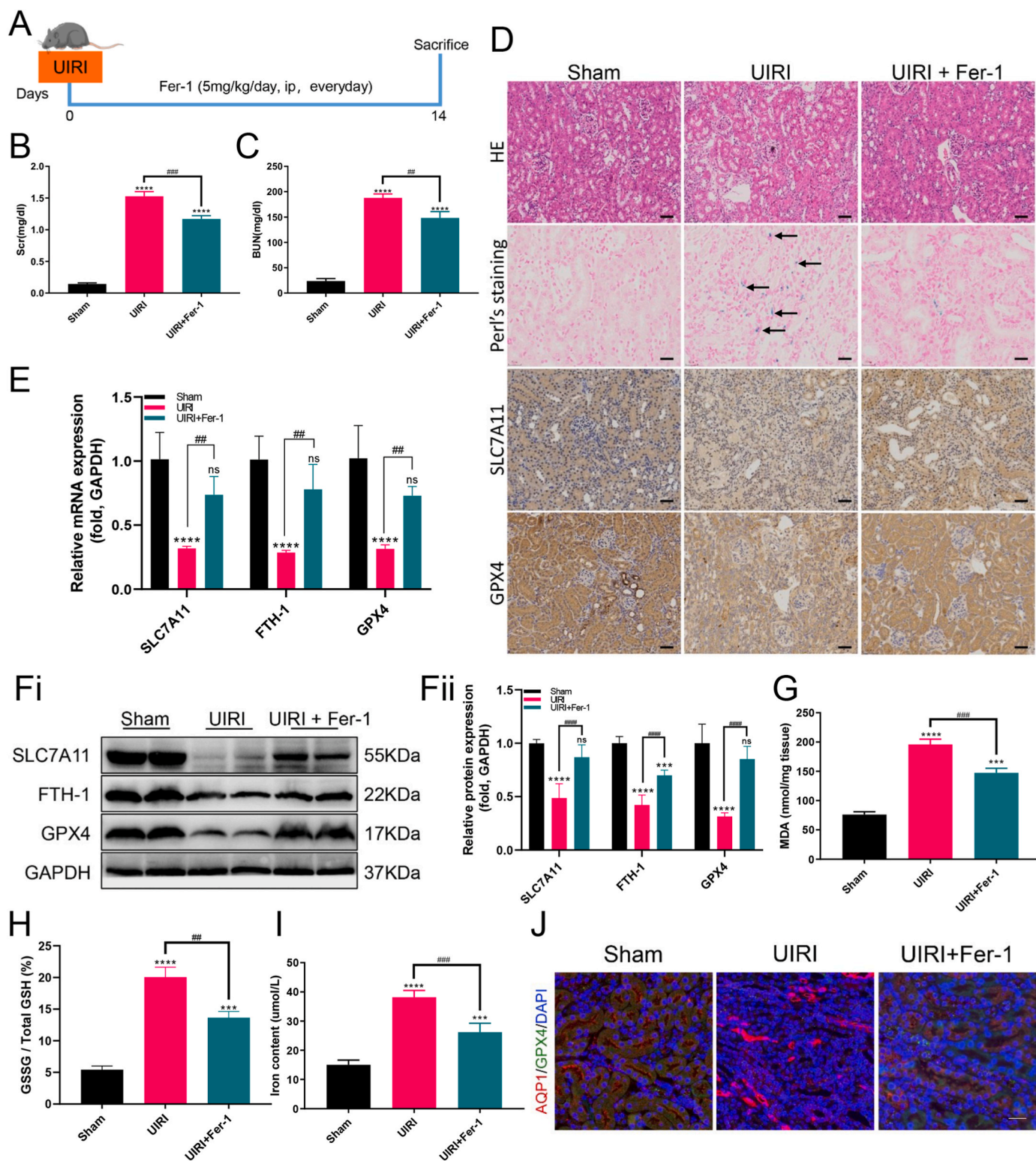
Fig. 5. UIRI induces ferroptosis in renal tubular epithelial cells. A. Diagram shows the animal experimental design. **B, C.** Serum creatinine (B) and blood urea nitrogen (C) levels in different groups as indicated (n = 3). **D.** Representative images of HE, Perl's staining, and immunohistochemical staining for SLC7A11 and GPX4 in UIRI or Fer-1 (5 mg/kg) treated mice kidneys. Scale bar = 50um. **E.** mRNA expression of SLC7A11, FTH-1, and GPX4 in UIRI or Fer-1 treated mice kidneys was measured by qRT-PCR (n = 3). **F.** Representative Western blotting (Fi) and quantitative data (Fii) show the protein expression of SLC7A11, FTH-1, and GPX4 in Fer-1 treated mice kidneys after UIRI. Relative expressions were expressed as fold induction over sham controls after normalization with GAPDH. ns, ***P < 0.001 and ****P < 0.0001 vs sham; ####P < 0.0001 vs UIRI group; ns, not significant (n = 4). **G-I.** MDA (G), GSSG/total GSH ratio (H), and Iron content (I) in different treated kidney tissues (n = 4, ***P < 0.001 and ****P < 0.0001 versus sham; ##P < 0.01 and ###P < 0.001 vs UIRI group). **J.** Double immunofluorescence staining demonstrates ferroptosis predominantly in the proximal tubular epithelium. Kidney sections were co-stained for AQP-1 (Red) and GPX4 (green), respectively. Scale bar = 50 μm.

expression in the UIRI group compared to the sham group, with corresponding decreases in mRNA and protein levels (Fig. 5D–F). Importantly, Fer-1 treatment alleviated these injuries, suggesting that UIRI may induce renal ferroptosis which is characterized by the accumulation of lipid peroxidation products, ferroptosis requires substantial iron levels [20]. Further analysis showed significant increases in MDA content and the GSSG/total GSH ratio in the UIRI group, which Fer-1 reversed (Fig. 5G and H). Additionally, an increase in renal iron concentration during UIRI was notably reduced following Fer-1 treatment (Fig. 5D and I). Immunofluorescence staining for Aquaporin-1 (AQP-1, tubular cell marker) and GPX4 in kidney tissues indicated that GPX4 levels in tubular cells were significantly diminished in the UIRI group compared to the sham group and were restored in the Fer-1 treated group (Fig. 5J), confirming that UIRI induces renal ferroptosis predominantly within TECs, the primary site of injury.

3.5. 3D-EVs can alleviate ferroptosis and EMT in NRK-52E cells induced by H/R in vitro

Renal TECs have been identified as the primary site of ferroptosis, suggesting that targeting TECs could mitigate renal IRI. Therefore, we proposed that 3D-EVs might attenuate renal IRI by modulating ferroptosis in TECs. To examine this hypothesis, NRK-52E cell injury was induced through H/R, followed by treatment with 2D- and 3D-EVs. As shown in Fig. 6A and B, the expression levels of SLC7A11, GPX4, and FTH-1, both mRNA and protein, were significantly reduced following H/R induction, an effect that was notably reversed upon 2D- and 3D-EVs treatment, with a better effect was observed in H/R+3D-EVs. Furthermore, the H/R group exhibited significant increases in MDA levels, ROS, and iron concentration, as depicted in Fig. 6C–F; however, these elevations were significantly attenuated by 2D- and 3D-EVs intervention, and 3D-EVs showed better results. These findings suggest that 3D-EVs can significantly mitigate ferroptosis in TECs induced by hypoxia/reoxygenation than 2D-EVs in vitro.

3.6. 3D-EVs can alleviate renal ischemia-reperfusion injury and fibrosis by inhibiting ferroptosis

To evaluate the potential of 3D-EVs in mitigating ferroptosis in UIRI-afflicted mice, we administered 2D- and 3D-EVs as a treatment (Fig. 7A). As shown in Fig. 7B-C, 3D-EVs significantly reinstated the expression of SLC7A11, FTH-1, and GPX4 at both the mRNA and protein levels than 2D-EVs, which UIRI had suppressed. Additionally, TUNEL staining revealed a marked reduction in cell apoptosis rates in 2D- and 3D-EVs treated UIRI mice (Fig. S2). As shown in Fig. 7D, perl's staining showed that the blue particles that appeared in UIRI, which are indicative of iron ion deposition, were reduced after treatments 2D- and 3D-EVs, and the reduction was more pronounced after 3D-EVs treatment. Immunohistochemical analyses further showed that 3D-EVs treatment mitigated the UIRI-induced overexpression of fibronectin, collagen I, and the low expression of GPX4 than 2D-EVs. Moreover, immunofluorescence staining verified the restoration of GPX4 expression in UIRI mice post 2D- and 3D-EVs treatment, affirming that ferroptosis primarily occurs within TECs and 3D-EVs could attenuate UIRI-induced renal tubular injury (AQP-1 expression level) and ferroptosis (GPX4 expression level) (Fig. 7E). These findings substantiate the efficacy of 3D-EVs was superior to 2D-EVs in alleviating ferroptosis and fibrosis in renal TECs induced by UIRI.

3.7. KLF15 plays a key role in 3D-EVs therapy for renal UIRI induced-ferroptosis

To unravel the mechanism underlying the therapeutic effects of 3D-EVs on renal UIRI-induced ferroptosis, RNA sequencing was utilized to assess mRNA expression changes in NRK-52E cells subjected to H/R and H/R + 3D-EVs. As shown in Fig. 8A, the Venn diagram showed the total

changes of NRK-52E cells' differentially expressed genes (DEGs) after H/R, 2D- and 3D-EVs treatment. As shown in the volcano plots, there were 1041 downregulated and 860 upregulated DEGs between the control and H/R groups (Fig. 8B). These genes were predominantly associated with fatty acid metabolism and ferroptosis, as revealed through the KEGG pathway and GSEA analysis (Fig. 8C and D). Moreover, the volcano plots showed there were 75 downregulated and 125 upregulated DEGs between the H/R and H/R + 2D-EVs groups (Fig. 8E), as well as 94 downregulated and 82 upregulated DEGs between the H/R group and the H/R + 3D-EVs groups (Fig. 8F). To further clarify the key DEGs that were superior to 2D-EVs in 3D-EVs, we identified common DEGs only in the Ctrl vs H/R group and H/R vs H/R+3D-EVs group through the Venn diagram, which is indicated with the red box in Fig. 8A. This approach led to the identification of 46 critical genes (Fig. S3). Specific genes associated with ferroptosis, including VDR, HMGA2, MGST1, KLF15, IL-33, HADH, and LCN2, were confirmed and displayed in a gene heatmap (Fig. 8G). qPCR experiments were conducted to validate these gene expression patterns in cells treated with H/R or H/R + 3D-EVs, yielding results consistent with the RNA sequencing data, except for VDR and IL33 mRNA levels (Fig. S4). Krüppel-Like Factor 15 (KLF15) is a key regulator of renal injury in TECs, but whether 3D-EVs could regulate KLF15 to alleviate TECs ferroptosis has not been studied [21]. Notably, KLF15, a pivotal regulator of renal injury in tubular epithelial cells (TECs), exhibited a marked decrease in mRNA expression in H/R-induced NRK-52E cells and UIRI mouse kidneys compared to control or sham groups. However, a substantial elevation in KLF15 protein expression was observed in the H/R + 3D-EVs and UIRI + 3D-EVs groups relative to the H/R or UIRI groups (Fig. 8H, I, J, K), as corroborated by immunohistochemical and immunofluorescence staining (Fig. 8L). These above results suggest that 3D-EVs exert therapeutic effects on UIRI-induced kidney injury by influencing the expression of KLF15 protein but not mRNA. Therefore, we hypothesize that 3D-EVs may exert a protective effect against UIRI-induced ferroptosis in renal TECs by delivering KLF15 protein.

3.8. 3D-EVs may deliver KLF15 to alleviate UIRI-induced renal injury and ferroptosis

To ascertain whether 3D-EVs delivering KLF15 protein exert therapeutic effects on UIRI, we analyzed KLF15 protein expression in AD-MSCs and 3D-EVs. As shown in Fig. 9A, both MSCs and 3D-EVs express KLF15 protein, whereas KLF15 protein expression was not detected in the EVs-free conditioned medium. Additionally, KLF15 protein expression in AD-MSCs and 3D-EVs was assessed via ELISA assay (Fig. 9B), revealing that, at equivalent protein concentrations, AD-MSCs contained approximately 322 pg/ml of KLF15 protein, in contrast to approximately 77 pg/ml in 3D-EVs, approximately one-fourth of the cellular content. However, the link between KLF15 and ferroptosis remains unclear. To explore whether ferroptosis presence influences KLF15 mRNA expression, NRK-52E cells were treated with 3D-EVs in the absence of H/R. As depicted in Fig. S5A, a marginal increase in KLF15 mRNA was observed in the 3D-EVs group compared to the control group, though not statistically significant. Conversely, Western blot analysis revealed a notable increase in KLF15 protein expression following 3D-EVs treatment (Fig. S5B). Moreover, the impact of 3D-EVs on ferroptosis was examined, showing that 3D-EVs induced upregulation of SLC7A11 and GPX4 expression in NRK-52E cells, thereby affirming the role of 3D-EVs in mitigating ferroptosis (Fig. S5C). These findings imply that 3D-EVs might function by delivering KLF15 protein to NRK-52E cells.

To further analysis of the relationship between KLF15 and ferroptosis through transfection of NRK-52E cells with KLF15 overexpression plasmid revealed that KLF15 overexpression significantly elevated KLF15 mRNA and protein expression (Fig. 9C and D), indicating effective transfection. KLF15 overexpression also led to increased expression of SLC7A11 and GPX4 relative to the control group (Fig. S5D),
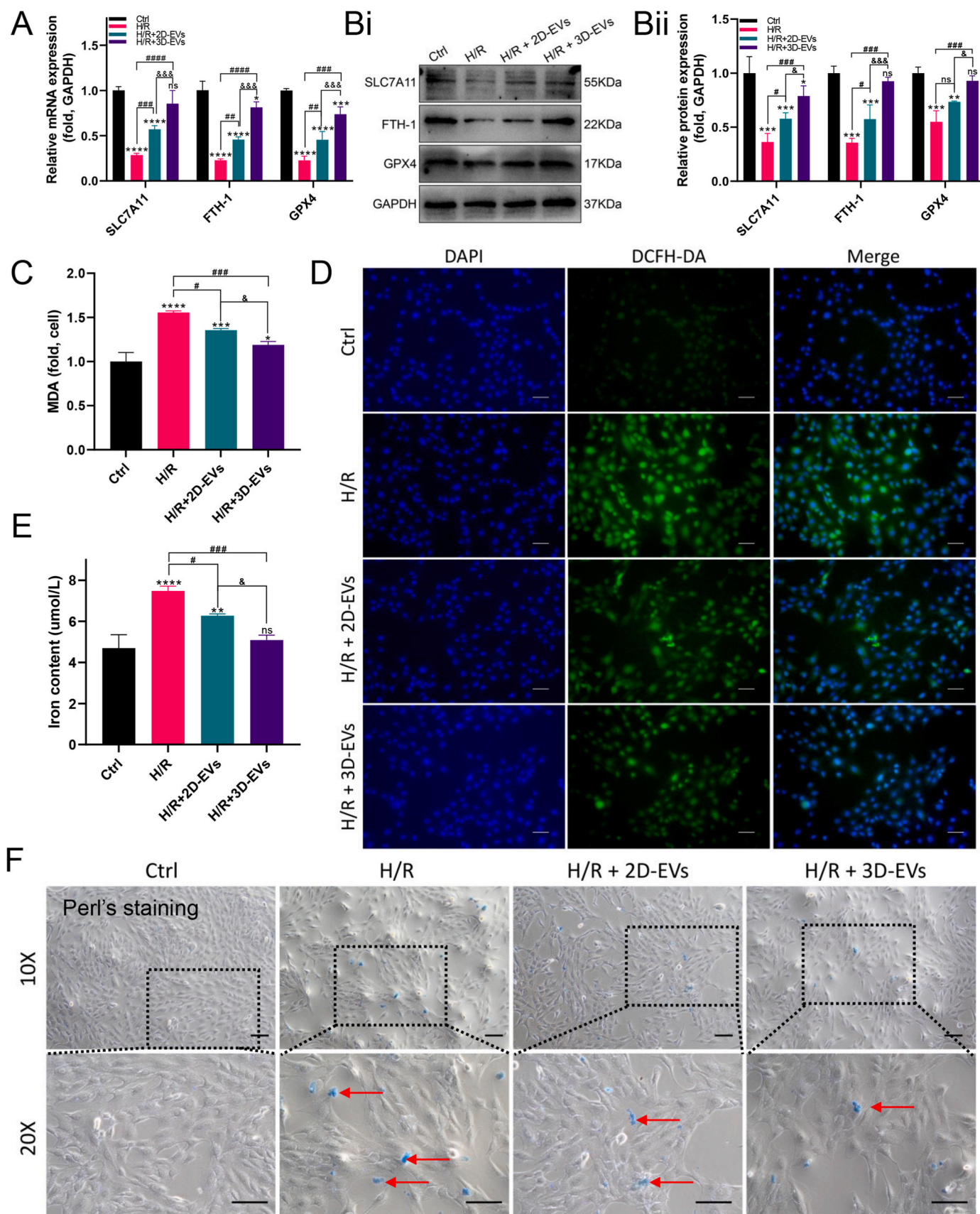
(caption on next page)

Fig. 6. 3D-EVs can alleviate ferroptosis and EMT in NRK-52E cells induced by H/R in vitro. **A.** mRNA expression of SLC7A11, FTH-1, and GPX4 in H/R,2D- and 3D-EVs treated NRK-52E cells was measured by qRT-PCR (n = 3). **B.** Representative Western blotting (Bi) and quantitative data (Bii) show the protein expression of SLC7A11, FTH-1, and GPX4 in 2D- and 3D-EVs treated NRK-52E cells after H/R. Relative expressions were expressed as fold induction over controls after normalization with GAPDH. ns, *P < 0.05, **P < 0.01, ***P < 0.001, and ****P < 0.0001 vs control; #P < 0.05, ##P < 0.01, ###P < 0.001, and ####P < 0.0001 vs H/R group; &P < 0.05 and &&P < 0.001 vs UIRI+3D-EVs group; ns, not significant (n = 4). **C, D.** MDA (C) and ROS production (D) in different treated NRK-52E cells (n = 3, *P < 0.05, ***P < 0.001, and ****P < 0.0001 versus control; #P < 0.05 and ###P < 0.01 vs H/R group; &P < 0.05 vs UIRI+3D-EVs group; Scale bar = 50 μm). **E, F.** Iron content and Perl's staining of NRK-52E cells after different treatments (n = 3, ns, **P < 0.01, and ****P < 0.0001 versus control; #P < 0.05 and ###P < 0.01 vs H/R group; &P < 0.05 vs UIRI+3D-EVs group; Scale bar = 50 μm).
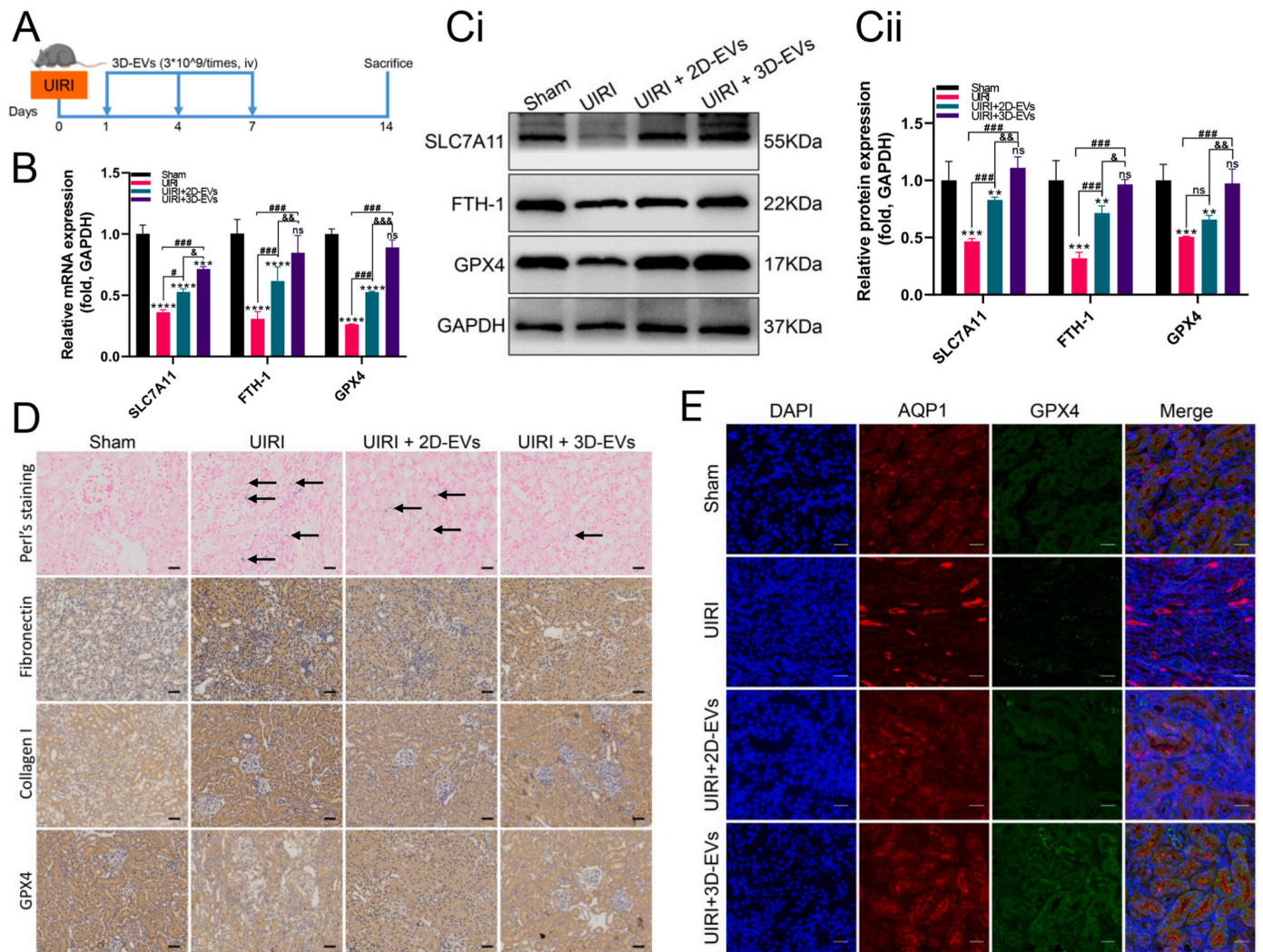

Fig. 7. 3D-EVs can alleviate renal ischemia-reperfusion injury and fibrosis by inhibiting ferroptosis. **A.** Diagram shows the animal experimental design. Blue arrows indicate the time points when 3D-EVs (3*10^9 particles/times) were injected intravenously. **B.** mRNA expression of SLC7A11, FTH-1, and GPX4 in UIRI,2D- and 3D-EVs treated mice kidneys was measured by qRT-PCR (n = 3). **C.** Representative Western blotting (Ci) and quantitative data (Cii) show the protein expression of SLC7A11, FTH-1, and GPX4 in 2D- and 3D-EVs treated mice kidneys after UIRI. Relative expressions were expressed as fold induction over sham controls after normalization with GAPDH. ns, **P < 0.01 and ***P < 0.001 vs sham; ns, ###P < 0.001 vs UIRI group; &P < 0.05, and &&P < 0.01 vs UIRI+3D-EVs group; ns, not significant (n = 3). **D.** Representative images of perl's staining and immunohistochemical staining for Fibronectin, Collagen I and GPX4 in UIRI, 2D- and 3D-EVs treated mice kidneys. Scale bar = 50um. **E.** Double immunofluorescence staining demonstrates ferroptosis in the proximal tubular epithelium was alleviated after 2D- and 3D-EVs were treated. Kidney sections were co-stained for AQP-1 (Red) and GPX4 (green), respectively. Scale bar = 50 μm.

suggesting KLF15's role in anti-ferroptosis. Additionally, in the H/R + OE group, protein levels of SLC7A11 and GPX4 were augmented compared to the H/R group (Fig. 9E), aligning with immunocyto-chemistry staining results (Fig. 9F). Subsequent experiments with KLF15 siRNA in NRK-52E cells showed a significant reduction in KLF15 mRNA and protein expression (Fig. 9G and H), with corresponding decreases in SLC7A11 and GPX4 expression (Fig. S5E), indicating that KLF15 downregulation may trigger ferroptosis in TECs. The application of Fer-1 to siKLF15-transfected NRK-52E cells partially reversed the suppression

of SLC7A11 and GPX4 protein expression (Fig. 9I), corroborated by immunocytochemistry staining (Fig. 9J). Therefore, KLF15 might miti-gate UIRI-induced renal injury and H/R-induced NRK-52E cell injury by modulating the ferroptosis signaling pathway. Collectively, these find-ings suggest that 3D-EVs' efficacy in treating renal UIRI could be ascribed to their delivery of KLF15 protein, highlighting 3D-EVs/KLF15 as a promising therapeutic strategy for UIRI management.
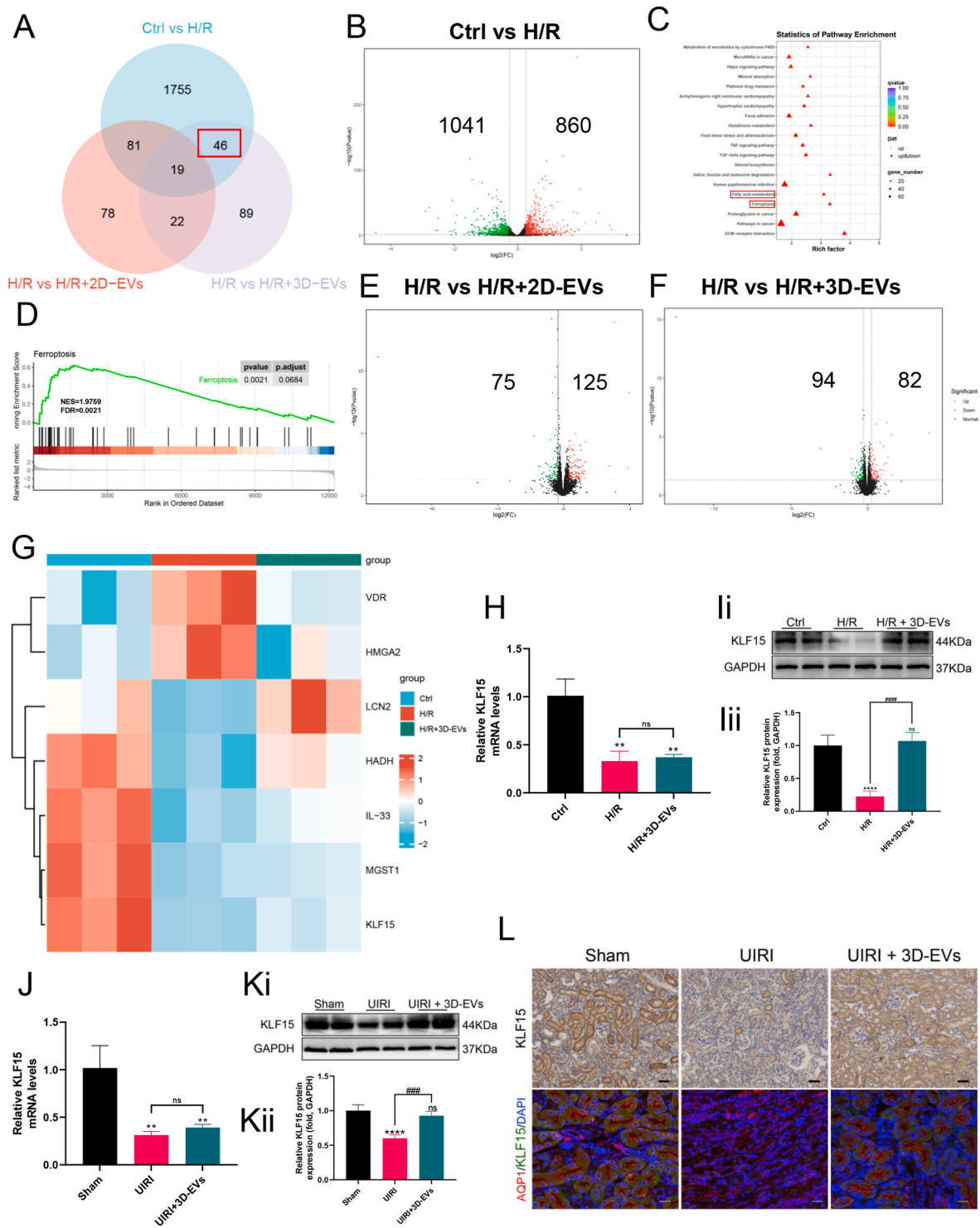
Fig. 8. KLF15 plays a key role in 3D-EVs therapy for renal UIRI-induced ferroptosis. A. Venn diagram of NRK-52E cells' DEGs after H/R, 2D- and 3D-EVs treatment. **B.** The volcano plots were analyzed between the Control and H/R groups. **C.** Kyoto Encyclopedia of Genes and Genomes (KEGG) enrichment analyses of tubular epithelial cells DEGs after mRNA sequencing between the Control and H/R groups, including the top 20 representative upregulated or downregulated signaling pathways. **D.** Gene Set Enrichment Analysis (GSEA) enrichment plots for two gene sets from the hallmark database associated with ferroptosis are shown. **E.** The volcano plots were analyzed between the H/R and H/R + 2D-EVs groups. **F.** The volcano plots analyzed between the H/R and H/R + 3D-EVs groups. **G.** Heatmaps of screened DEGs involved in the ferroptosis process of tubular epithelial cells. **H, J.** mRNA expression of KLF15 in H/R treated NRK-52E cells (H) or UIRI mice kidneys (J) were measured by qRT-PCR. **P < 0.0001 vs sham, ns vs UIRI group; ns, not significant (n = 3). **I.** Representative Western blotting (Ii) and quantitative data (Iii) show the protein expression of KLF15 in 3D-EVs treated NRK-52E cells after H/R. Relative expressions were expressed as fold induction over controls after normalization with GAPDH. ns, ****P < 0.0001 vs control; ####P < 0.0001 vs H/R group; ns, not significant (n = 4). **K.** Representative Western blotting (Ki) and quantitative data (Kii) show the protein expression of KLF15 in 3D-EVs treated mice kidneys after UIRI. Relative expressions were expressed as fold induction over sham controls after normalization with GAPDH. ns, ****P < 0.0001 vs sham; ###P < 0.001 vs UIRI group; ns, not significant (n = 4). **L.** Representative images of immunohistochemical staining and double immunofluorescence staining demonstrate KLF15 predominantly expressed in the proximal tubular epithelium. Kidney sections were co-stained for AQP-1 (Red) and KLF15 (green), respectively. Scale bar = 50 μm.
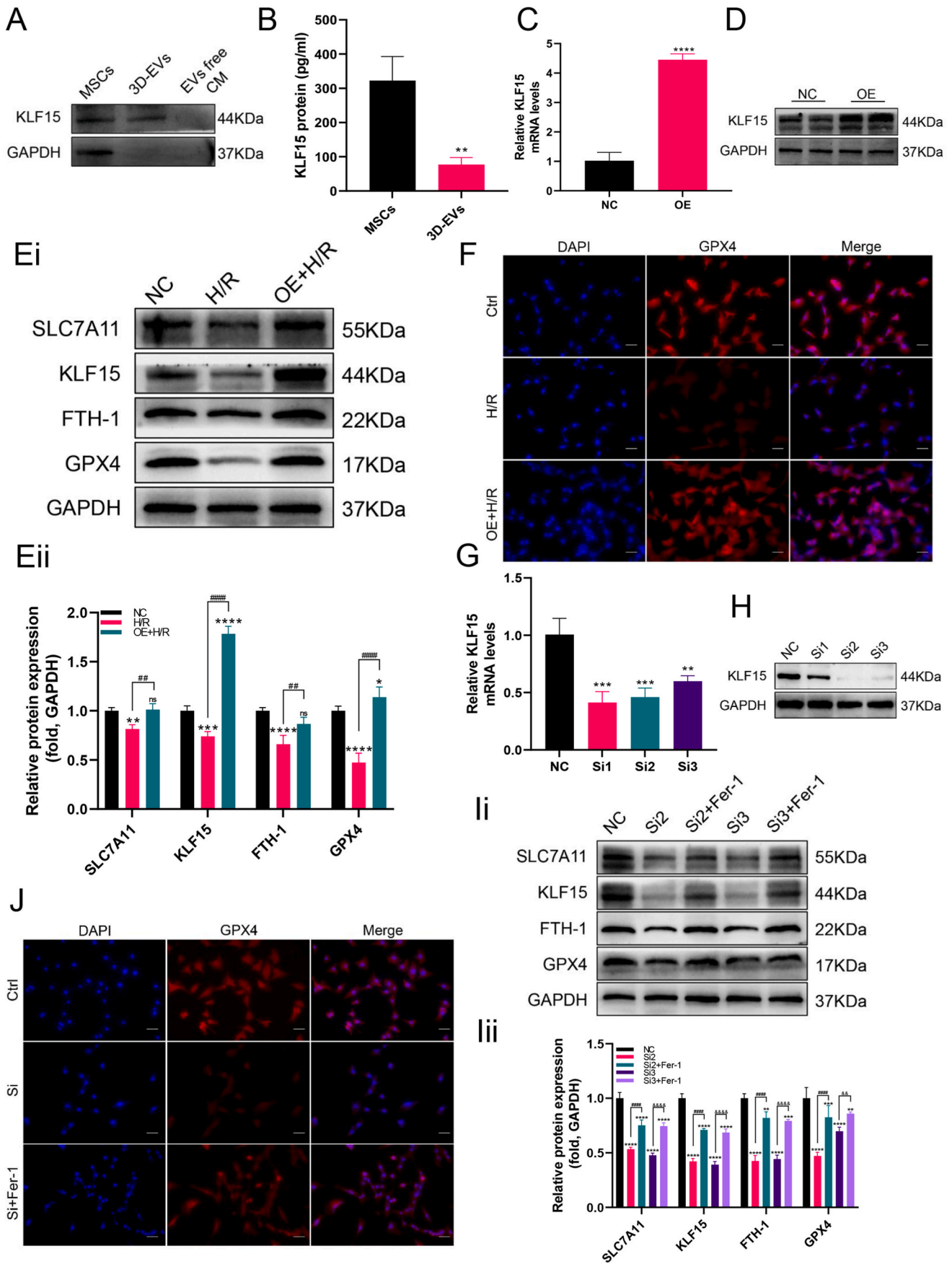
(caption on next page)

Fig. 9. 3D-EVs may deliver KLF15 to alleviate UIRI-induced renal injury and ferroptosis.

A, B. Representative western blotting (A) and ELISA quantification (B) show the protein expression of KLF15 in MCS and their derived 3D-EVs. **C, D.** mRNA (C) and protein (D) expression of KLF15 in NRK-52E cells after transfected with KLF15 overexpressed plasmid. ****P < 0.0001 compared with NC group (n = 3). **E.** Representative Western blotting (Ei) and quantitative data (Eii) show the protein expression of SLC7A11, KLF15, FTH-1, and GPX4 in H/R or overexpressed plasmid treated NRK-52E cells. Relative expressions were expressed as fold induction over controls after normalization with GAPDH. ns, **P < 0.01, ***P < 0.001 and ****P < 0.0001 vs NC group; ##P < 0.01, ####P < 0.0001 vs UIRI group (n = 3). **F.** Immunofluorescence staining shows the protein expression of GPX4 in H/R or overexpressed plasmid treated NRK-52E cells. Scale bar = 50 μm. **G, H.** mRNA (G) and protein (H) expression of KLF15 in NRK-52E cells after transfected with small interfering RNA KLF15 (siKLF15). **P < 0.01, ****P < 0.0001 compared with NC group (n = 3). **I.** Representative Western blotting (Ii) and quantitative data (Iii) show the protein expression of SLC7A11, KLF15, FTH-1 and GPX4 in siKLF15 or Fer-1 treated NRK-52E cells. Relative expressions were expressed as fold induction over controls after normalization with GAPDH. ns, **P < 0.01, ***P < 0.001 and ****P < 0.0001 vs NC group; ####P < 0.0001 vs si2 group; &&P < 0.01, &&&&P < 0.0001 vs si3 group (n = 3). **J.** Immunofluorescence staining shows the protein expression of GPX4 in siKLF15 or Fer-1 treated NRK-52E cells. Scale bar = 50 μm.

4. Discussion

In this study, we have innovatively integrated a modified high-efficiency and high-quality extracellular vesicles production technology with a tail vein injection method to assess its therapeutic potential for unilateral renal ischemia-reperfusion injury. The extracellular vesicles produced through this advanced methodology were termed 3D-EVs, and our findings indicate that 3D-EVs exhibit superior therapeutic effects compared to traditional 2D-EVs in both in vitro H/R induced TECs and in vivo UIRI mouse models. Further investigation into the action mechanism of 3D-EVs on UIRI treatment suggests that 3D-EVs potentially convey KLF15, which mitigates renal ischemia-reperfusion injury and alleviates H/R-induced injuries in NRK-52E cells by targeting ferroptosis. In vitro analyses demonstrated that 3D-EVs enhance KLF15 expression in NRK-52E cells via the transfer of EV-contained KLF15, ameliorating the suppression of SLC7A11 and GPX4. This led to a reduction in ROS, Fe2+, vimentin, and α-SMA in NRK-52E cells. In vivo, 3D-EVs were shown to alleviate UIRI by inhibiting ferroptosis and reducing extracellular matrix deposition. In summary, 3D-EVs offer a more effective approach to mitigating UIRI-induced renal injury and fibrosis than 2D-EVs, primarily by inhibiting ferroptosis in NRK-52E cells through the EVs/KLF15/SLC7A11/GPX4 signaling pathway.

Biophysical cues within the cellular microenvironment significantly affect cell behavior and function through mechanotransduction, with cells cultured in various environments displaying distinct functionalities and capacities for extracellular vesicle secretion. Wu et al. [22] reported that a stiff ECM activates the AKT signaling pathway in cancer cells, thereby promoting GTP loading to Rab 8, which in turn drives the secretion of extracellular vesicles. These secreted vesicles from cancer cells lead to alterations in the tumor microenvironment, facilitating tumor growth. Li et al. [10]investigated the effect of 3D micropattern-induced mechanotransduction on human mesenchymal stem cells, demonstrating that forces from 3D micropatterns influence the spatial reorganization of the cytoskeleton. This results in nuclear flattening and stretching of nuclear pores, which enhances the nuclear import of YES-associated protein (YAP) and subsequently improves MSCs paracrine functions. In our study, we introduced a coaxial bio-printed microfiber technology for MSCs cultivation and extracellular vesicle production. This technology, featuring a unique hollow tube topology, enables high-density cell cultivation and the formation of tissue-like microenvironments, thereby facilitating efficient extracellular vesicle production. The microfibers produced offer several advantages over conventional cultivation methods [11], including providing a natural environment for cell interaction and self-assembly within a soft 3D matrix, promoting secretion by maintaining cell stemness and enhancing secretory capacity, allowing for the cultivation of cell clusters at high densities, enriching cellular products through concentration effects and continuous harvesting, and producing high-quality extracellular vesicles with a rich composition of cargo contents. Consequently, the cultivation environment significantly influences the secretion capacity of extracellular vesicles. Moreover, three-dimensional microenvironments prove advantageous for the efficient and high-quality production of stem cell-derived extracellular vesicles. Nonetheless, research on the application of such efficiently

produced extracellular vesicles in disease contexts, particularly in UIRI, remains scarce.

UIRI is recognized as a progressive disease for which effective treatments remain elusive [23–25]. MSC-EVs have demonstrated therapeutic potential across a spectrum of renal disorders, including ischemia-reperfusion injury, unilateral ureteral obstruction (UUO), and renal cell carcinoma [26]. Despite these advancements, the precise mechanisms by which MSC-EVs mitigate UIRI are yet to be fully understood. Compounding this challenge is the constrained production and compromised functionality of extracellular vesicles, which significantly impede the advancement of research and the development of efficient, cost-effective EV-based therapeutics. By leveraging coaxial bioprinting technology, 3D-EVs offer a solution to these limitations, exhibiting superior bioactivity through enhanced cell proliferation, migration, and angiogenesis [11]. This study employs coaxial bioprinting technology for the production of 3D-EVs and conducts a comparative analysis of their therapeutic efficacy against traditional 2D-EVs. Our findings indicate that 3D-EVs yield superior therapeutic outcomes compared to 2D-EVs, as evidenced by improved renal function and reduced extracellular matrix deposition in both in vitro and in vivo models of UIRI.

Ferroptosis, a recently identified programmed cell death mechanism [19], is intricately linked to iron metabolism and plays a pivotal role in the onset and progression of various renal diseases, including ischemia-reperfusion injury-induced AKI [27], renal fibrosis [28], renal cell carcinoma [29] and cisplatin-induced renal injury [30]. Fer-1, a specific inhibitor of ferroptosis, attenuates ferroptosis-induced renal injury by inhibiting TECs lipid peroxidation and ferrous ion deposition. TECs are essential in the development of renal IRI, and our findings indicate that renal ferroptosis predominantly occurs in TECs, as evidenced by co-immunofluorescence staining of AQP-1 and GPX4. Thus, targeting TEC ferroptosis emerges as a potential therapeutic strategy to mitigate various renal injuries. SLC7A11, a membrane antiporter facilitating the exchange of intracellular glutamate for extracellular cysteine, plays a crucial role in protecting cells from oxidative stress and ferroptosis via GPX4 activity [19]. Consequently, modulation of the SLC7A11/GPX4 axis represents a promising approach to UIRI treatment. Our research further validates that 3D-EVs can alleviate H/R-induced injury in NRK-52E cells and UIRI-induced renal injury, as demonstrated by the reduction in intracellular ROS and iron (Fe2+) levels and the upregulation of ferroptosis defense biomarkers, SLC7A11 and GPX4. These findings underscore the potential of 3D-EVs to counteract H/R-induced NRK-52E cell injury and UIRI-induced renal injury by inhibiting ferroptosis, thereby offering a therapeutic benefit in renal damage management. Additionally, UIRI and UUO models significantly contribute to renal fibrosis, with injured renal tissues promoting EMT of tubular cells and fibroblast proliferation through paracrine mechanisms, leading to the production of vimentin, α-smooth muscle actin (α-SMA), and collagen I [31]. Our study corroborates that hypoxic conditions or UIRI can exacerbate EMT in TECs and renal fibrosis. Conversely, treatment with 3D-EVs under hypoxia or UIRI conditions notably inhibits EMT in TECs and decelerates renal fibrosis progression.

Extracellular vesicles, encompassing DNA, RNA, proteins, and lipids, have the capability to be transferred to another cell, where they can exert functional effects in contexts such as renal injury and fibrosis

[32–34]. While much of the existing research has concentrated on the role of RNA delivered by extracellular vesicles in renal diseases, the delivery of proteins remains comparatively underexplored. Krüppel-Like Factor 15 (KLF15), a zinc-finger transcription factor abundantly present in the proximal tubule [35,36], has been identified as a key role in renal interstitial fibrosis and glomerulosclerosis [37,38]. A deficiency in KLF15 has been associated with increased susceptibility to renal damage. Notably, levels of KLF15 are significantly diminished in proximal tubule cells following aristolochic acid I (AAI)-induced AKI, and the specific loss of KLF15 in these cells exacerbates AKI and fibrosis [21,39]. Our RNA-sequencing analysis revealed a downregulation of KLF15 in NRK-52E cells subjected to H/R and its subsequent upregulation following treatment with 3D-EVs, suggesting a crucial role for KLF15 in the context of UIRI. However, while significant upregulation of KLF15 protein was observed, especially localized within renal tubular cells, KLF15 mRNA levels did not exhibit a corresponding increase in the H/R + 3D-EVs or UIRI + 3D-EVs groups compared to the H/R or UIRI groups. Consequently, we propose that the therapeutic effect of 3D-EVs in UIRI may be mediated through the delivery of KLF15 protein.

We delved further into the mechanisms underlying the renal protective effects conferred by KLF15 derived from 3D-EVs. Initially, we established through Western blot and ELISA analyses that KLF15 is enriched in 3D-EVs. We hypothesized that ferroptosis could suppress the significant upregulation of KLF15 mRNA, leading us to treat TECs exclusively with 3D-EVs. This treatment did not notably enhance KLF15 mRNA expression in NRK-52E cells, although it significantly increased the protein levels of KLF15, SLC7A11, and GPX4, thereby suggesting that ferroptosis does not inhibit KLF15 mRNA expression. To elucidate the relationship between KLF15 and ferroptosis further, we manipulated NRK-52E cells with KLF15 overexpression plasmids and siRNA, observing a consistent inverse association between KLF15 expression and ferroptosis markers. These observations indicate that 3D-EVs may counteract ferroptosis by modulating SLC7A11 and GPX4 levels through KLF15 delivery. Consequently, engineered extracellular vesicles harboring overexpressed KLF15 emerge as a novel therapeutic strategy for addressing UIRI-induced renal diseases.

In summary, our study revealed that extracellular vesicles derived from bioprinted MSC microfibers surpass the therapeutic efficacy of 2D-EVs in mitigating H/R-induced NRK-52E cell injury or UIRI-induced renal injury. The primary mechanism involves 3D-EVs delivering KLF15 to tubular epithelial cells, thereby inhibiting ferroptosis through the upregulation of SLC7A11 and GPX4. This research offers novel insights into stem cell culture, and extracellular vesicle extraction, and elucidates various mechanisms through which 3D-EVs afford protection against UIRI-induced renal injury.

Data availability

Data will be made available on request.

Ethics approval and consent to participate

All experiments involving animals were conducted according to the ethical policies and procedures approved by the ethics committee of the sixth affiliated hospital of Sun-Yat Sen University (Approval no. IACUC-2021092902).

CRediT authorship contribution statement

Qiang Guo: Writing – original draft, Visualization, Validation, Methodology, Investigation. **Jianwei Chen:** Writing – review & editing, Methodology, Conceptualization. **Jianjian Wu:** Writing – review & editing, Methodology, Data curation. **Zijun Mo:** Validation, Formal analysis. **Lei Ye:** Formal analysis. **Wenwen Zhong:** Formal analysis. **Yi Zhang:** Conceptualization. **Huajian Lai:** Formal analysis. **Yifei Zhang:** Formal analysis. **Jianguang Qiu:** Supervision, Project administration,

Funding acquisition. **Tao Xu:** Supervision, Resources, Funding acquisition, Conceptualization. **Dejuan Wang:** Validation, Supervision, Resources, Project administration, Conceptualization.

Declaration of competing interest

The authors declare the following personal relationships which may be considered as potential competing interests: Yi Zhang is currently employed by Huaqing Zhimei (Shenzhen) Biotechnology Co., Ltd.

Acknowledgments

Appendix A. Supplementary data

Supplementary data to this article can be found online at https://doi.org/10.1016/j.bioactmat.2024.08.011.

References

[1] D.M. Hoang, P.T. Pham, T.Q. Bach, A.T.L. Ngo, Q.T. Nguyen, T.T.K. Phan, et al., Stem cell-based therapy for human diseases, Signal Transduct. Targeted Ther. 7 (1) (2022) 272.

[2] Y. Wang, S.K. Shan, B. Guo, F. Li, M.H. Zheng, L.M. Lei, et al., The multi-therapeutic role of MSCs in diabetic nephropathy, Front. Endocrinol. 12 (2021) 671566.

[3] X. Xie, X. Yang, J. Wu, S. Tang, L. Yang, X. Fei, et al., Exosome from indoleamine 2,3-dioxygenase-overexpressing bone marrow mesenchymal stem cells accelerates repair process of ischemia/reperfusion-induced acute kidney injury by regulating macrophages polarization, Stem Cell Res. Ther. 13 (1) (2022) 367.

[4] Y. Zhou, H. Xu, W. Xu, B. Wang, H. Wu, Y. Tao, et al., Exosomes released by human umbilical cord mesenchymal stem cells protect against cisplatin-induced renal oxidative stress and apoptosis in vivo and in vitro, Stem Cell Res. Ther. 4 (2) (2013) 34.

[5] W. Liu, C. Hu, B. Zhang, M. Li, F. Deng, S. Zhao, Exosomal microRNA-342-5p secreted from adipose-derived mesenchymal stem cells mitigates acute kidney injury in sepsis mice by inhibiting TLR9, Biol. Proced. Online 25 (1) (2023) 10.

[6] D. Zheng, H. Ruan, W. Chen, Y. Zhang, W. Cui, H. Chen, et al., Advances in extracellular vesicle functionalization strategies for tissue regeneration, Bioact. Mater. 25 (2023) 500–526.

[7] M. Liu, H. Lutz, D. Zhu, K. Huang, Z. Li, P.C. Dinh, et al., Bispecific antibody inhalation therapy for redirecting stem cells from the lungs to repair heart injury, Adv. Sci. 8 (1) (2020) 2002127.

[8] R.A. Haraszti, R. Miller, M. Stoppato, Y.Y. Sere, A. Coles, M.C. Didiot, et al., Exosomes produced from 3D cultures of MSCs by tangential flow filtration show higher yield and improved activity, Mol. Ther. : the journal of the American Society of Gene Therapy 26 (12) (2018) 2838–2847.

[9] D.B. Patel, C.R. Luthers, M.J. Lerman, J.P. Fisher, S.M. Jay, Enhanced extracellular vesicle production and ethanol-mediated vascularization bioactivity via a 3D-printed scaffold-perfusion bioreactor system, Acta Biomater. 95 (2019) 236–244.

[10] Y. Li, Z. Zhong, C. Xu, X. Wu, J. Li, W. Tao, et al., 3D micropattern force triggers YAP nuclear entry by transport across nuclear pores and modulates stem cells paracrine, Natl. Sci. Rev. 10 (8) (2023) nwad165.

[11] J. Chen, D. Zhou, Z. Nie, L. Lu, Z. Lin, D. Zhou, et al., A scalable coaxial bioprinting technology for mesenchymal stem cell microfiber fabrication and high extracellular vesicle yield, Biofabrication 14 (1) (2021).

[12] J. Li, F. Cao, H.L. Yin, Z.J. Huang, Z.T. Lin, N. Mao, et al., Ferroptosis: past, present and future, Cell Death Dis. 11 (2) (2020) 88.

[13] Y. Tan, Y. Huang, R. Mei, F. Mao, D. Yang, J. Liu, et al., HucMSC-derived exosomes delivered BECN1 induces ferroptosis of hepatic stellate cells via regulating the xCT/GPX4 axis, Cell Death Dis. 13 (4) (2022) 319.

[14] L. Ni, C. Yuan, X. Wu, Targeting ferroptosis in acute kidney injury, Cell Death Dis. 13 (2) (2022) 182.

[15] K. Xiangkai, Z. Delong, H. Ying, L. Chang, Z. Yi, W. Yu, et al., Melt electrowriting (MEW)-PCL composite Three-Dimensional exosome hydrogel scaffold for wound healing, Mater. Des. 238 (2024) 112717.

[16] A. Eirin, X.Y. Zhu, A.S. Puranik, H. Tang, K.A. McGurren, A.J. van Wijnen, et al., Mesenchymal stem cell-derived extracellular vesicles attenuate kidney inflammation, Kidney Int. 92 (1) (2017) 114–124.

[17] A. Ranghino, S. Bruno, B. Bussolati, A. Moggio, V. Dimuccio, M. Tapparo, et al., The effects of glomerular and tubular renal progenitors and derived extracellular vesicles on recovery from acute kidney injury, Stem Cell Res. Ther. 8 (1) (2017) 24.

[18] G. Miotto, M. Rossetto, M.L. Di Paolo, L. Orian, R. Venerando, A. Roveri, et al., Insight into the mechanism of ferroptosis inhibition by ferrostatin-1, Redox Biol. 28 (2020) 101328.

[19] S.J. Dixon, K.M. Lemberg, M.R. Lamprecht, R. Skouta, E.M. Zaitsev, C.E. Gleason, et al., Ferroptosis: an iron-dependent form of nonapoptotic cell death, Cell 149 (5) (2012) 1060–1072.

[20] X. Jiang, B.R. Stockwell, M. Conrad, Ferroptosis: mechanisms, biology and role in disease, Nat. Rev. Mol. Cell Biol. 22 (4) (2021) 266–282.

[21] N. Suzuki, A. Kanai, Y. Suzuki, H. Ogino, H. Ochi, Adrenergic receptor signaling induced by Klf15, a regulator of regeneration enhancer, promotes kidney reconstruction, Proc. Natl. Acad. Sci. U.S.A. 119 (33) (2022) e2204338119.

[22] B. Wu, D.A. Liu, L. Guan, P.K. Myint, L. Chin, H. Dang, et al., Stiff matrix induces exosome secretion to promote tumour growth, Nat. Cell Biol. 25 (3) (2023) 415–424.

[23] X. Zhou, S. Zhao, W. Li, Y. Ruan, R. Yuan, J. Ning, et al., Tubular cell-derived exosomal miR-150-5p contributes to renal fibrosis following unilateral ischemia-reperfusion injury by activating fibroblast in vitro and in vivo, Int. J. Biol. Sci. 17 (14) (2021) 4021–4033.

[24] L.M. Black, J.M. Lever, A.M. Traylor, B. Chen, Z. Yang, S.K. Esman, et al., Divergent effects of AKI to CKD models on inflammation and fibrosis, Am. J. Physiol. Ren. Physiol. 315 (4) (2018) F1107, f18.

[25] R. Huang, P. Fu, L. Ma, Kidney fibrosis: from mechanisms to therapeutic medicines, Signal Transduct. Targeted Ther. 8 (1) (2023) 129.

[26] B.W. van Balkom, T. Pisitkun, M.C. Verhaar, M.A. Knepper, Exosomes and the kidney: prospects for diagnosis and therapy of renal diseases, Kidney Int. 80 (11) (2011) 1138–1145.

[27] K. Hosohata, T. Harnsirikarn, S. Chokesuwattanaskul, Ferroptosis: a potential therapeutic target in acute kidney injury, Int. J. Mol. Sci. 23 (12) (2022).

[28] B. Zhu, Y. Ni, Y. Gong, X. Kang, H. Guo, X. Liu, et al., Formononetin ameliorates ferroptosis-associated fibrosis in renal tubular epithelial cells and in mice with chronic kidney disease by suppressing the Smad 3/ATF3/SLC7A11 signaling, Life Sci. 315 (2023) 121331.

[29] Y. Zou, M.J. Palte, A.A. Deik, H. Li, J.K. Eaton, W. Wang, et al., A GPX4-dependent cancer cell state underlies the clear-cell morphology and confers sensitivity to ferroptosis, Nat. Commun. 10 (1) (2019) 1617.

[30] Z. Deng, Y. Wang, J. Liu, H. Zhang, L. Zhou, H. Zhao, et al., WBP2 restrains the lysosomal degradation of GPX4 to inhibit ferroptosis in cisplatin-induced acute kidney injury, Redox Biol. 65 (2023) 102826.

[31] X. Liu, J. Miao, C. Wang, S. Zhou, S. Chen, Q. Ren, et al., Tubule-derived exosomes play a central role in fibroblast activation and kidney fibrosis, Kidney Int. 97 (6) (2020) 1181–1195.

[32] M. Kosanović, A. Llorente, S. Glamočlija, J.M. Valdivielso, M. Bozic, Extracellular vesicles and renal fibrosis: an odyssey toward a new therapeutic approach, Int. J. Mol. Sci. 22 (8) (2021).

[33] L. Birtwistle, X.M. Chen, C. Pollock, Mesenchymal stem cell-derived extracellular vesicles to the rescue of renal injury, Int. J. Mol. Sci. 22 (12) (2021).

[34] X. Hu, N. Shen, A. Liu, W. Wang, L. Zhang, Z. Sui, et al., Bone marrow mesenchymal stem cell-derived exosomal miR-34c-5p ameliorates RIF by inhibiting the core fucosylation of multiple proteins, Mol. Ther. : the journal of the American Society of Gene Therapy 30 (2) (2022) 763–781.

[35] A.B. Bialkowska, V.W. Yang, S.K. Mallipattu, Krüppel-like factors in mammalian stem cells and development, Development 144 (5) (2017) 737–754.

[36] N.M. Pollak, M. Hoffman, I.J. Goldberg, K. Drosatos, Krüppel-like factors: crippling and un-crippling metabolic pathways, JACC Basic to translational science 3 (1) (2018) 132–156.

[37] X. Gao, G. Wu, X. Gu, L. Fu, C. Mei, Kruppel-like factor 15 modulates renal interstitial fibrosis by ERK/MAPK and JNK/MAPK pathways regulation, Kidney Blood Pres. Res. 37 (6) (2013) 631–640.

[38] X. Gu, S.K. Mallipattu, Y. Guo, M.P. Revelo, J. Pace, T. Miller, et al., The loss of Krüppel-like factor 15 in Foxd1(+) stromal cells exacerbates kidney fibrosis, Kidney Int. 92 (5) (2017) 1178–1193.

[39] S.E. Piret, A.A. Attallah, X. Gu, Y. Guo, N.A. Gujarati, J. Henein, et al., Loss of proximal tubular transcription factor Krüppel-like factor 15 exacerbates kidney injury through loss of fatty acid oxidation, Kidney Int. 100 (6) (2021) 1250–1267.